

Analysis of dynamical behaviour of full-floating disk thrust bearings

Steffen NITZSCHKE, Christian ZIESE, AND Elmar WOSCHKE

Institute of Mechanics, Otto-von-Guericke University, 39106 Magdeburg, Germany

Abstract. Full-floating ring bearings are state of the art at high speed turbomachinery shafts like in turbochargers. Their main feature is an additional ring between shaft and housing leading to two fluid films in serial arrangement. Analogously, a thrust bearing with an additional separating disk between journal collar and housing can be designed. The disk is allowed to rotate freely only driven by drag torques, while it is radially supported by a short bearing against the journal. This paper addresses this kind of thrust bearing and its implementation into a transient rotor dynamic simulation by solving the Reynolds PDE online during time integration. Special attention is given to the coupling between the different fluid films of this bearing type. Finally, the differences between a coupled and an uncoupled solution are discussed.

Key words: thrust bearings; full-floating; hydrodynamics; transient rotor dynamics; Elrod cavitation algorithm.

ABBREVIATIONS

CFD – computational fluid dynamics
FFD – full-floating disk
FFDB – full-floating disk (thrust) bearing
FFRB – full-floating ring (journal) bearing
FEM – finite element method
FVM – finite volume method
PDE – partial differential equation
SUPG – streamline upwind Petrov-Galerkin
THD – thermo-hydrodynamics

1. INTRODUCTION

In fast-rotating turbo machinery with significant axial loads, e.g. due to reaction forces of an axial turbine, sometimes thrust bearings with full-floating disk design are applied. This kind of bearing allows for larger tilting of the shaft and reduces the bearing friction losses as well as the wear due to lower relative velocities in the fluid films. Analogously to a full-floating ring bearing (radial support of a rotor), an additional disk is mounted between shaft and housing in a thrust bearing, cf. Fig. 1 left. This leads to two axial fluid films in serial arrangement. Due to the drag torques in both films the disk rotates with an intermediate angular velocity depending on the pressure distributions in both films. Besides, the disk has to be supported radially either against the rotating shaft or the housing. However, the oil supply of all films has to be assured. Usually, the oil is entering the bearing via the thrust film on the housing side and is then led through the radial film to the thrust film on the rotor side. Thus, the pressures in the films are coupled due to the boundary conditions at the interfaces. Another aspect is determined by the

friction losses in the films leading to temperature increase in the fluid films as well as in the bearing components, which interacts with the pressure distribution by means of the fluid viscosity.

1.1. Literature review

The archetype of the FFDB was clearly the FFRB, which has been under theoretical [1] and practical [2] investigation at least since 1947. The very first hint to a full-floating disk thrust bearing was given by Dworski [3] in 1964, who studied the application of FFRBs in gas turbines. In his conclusion a transfer of the working principle to a thrust bearing was recommended hoping that the advantages would be similar there. Harada [4] inserted a floating disk in a hydrostatic thrust bearing and observed a reduction of friction losses. But nowadays neither FFRBs nor FFDBs are established within gas turbines. Instead in some larger turbocharger designs with axial turbine, FFDBs have become state of the art [5, 6].

Theoretical investigations of FFDBs are relatively rare in the literature, but some works regarding combined thrust and radial bearings, which are similar to FFDBs, can be found. The majority assumes steady state operation conditions with a tribological scope: Engel [7] developed a CFD code, which is able to predict velocity, temperature and pressure distribution within the fluid gaps by solving the Navier Stokes, continuity and energy equation under steady state and adiabatic assumptions. Hagemann *et al.* [8] used an iterative coupling between two Reynolds-PDE solutions (including energy equation) based on an FVM algorithm one for the radial bearing and one for the thrust bearing, assuming a constant pressure and temperature in the interface between axial and radial gap. Jang *et al.* [9] have built a model of a herringbone grooved bearing with combined axial and radial gap, where the interaction between both fluid films is implicitly handled due to the FEM approach, which was applied to solve the Reynolds-PDE for both gap types. Analogously, Xiang *et al.* [10] developed an FVM code for coupled journal-

*e-mail: steffen.nitzschke@ovgu.de

Manuscript submitted 2021-03-31, revised 2021-07-12, initially accepted for publication 2021-08-16, published in December 2021

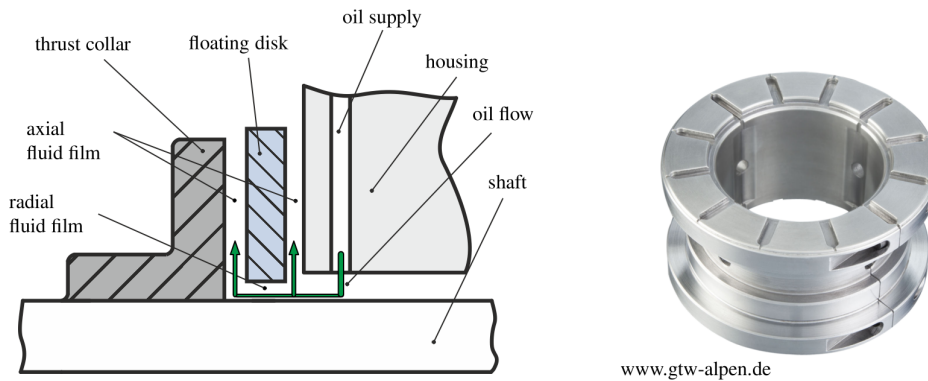


Fig. 1. Schematic design of full-floating disk thrust bearing (left) and picture of combined thrust and journal bearing (right)

thrust bearings with micro-groove structure, where Reynolds cavitation boundary conditions are applied. In contrast Luneno [11] has analysed the dynamic behaviour of a vertical hydro-turbogenerator rotor supported in combined bearings. The shaft including rotor is modeled with finite beam elements, but the bearings enter only as spring-damper combination in order to calculate the speed dependent eigenbehaviour.

Fischer *et al.* [5] deal directly with an FFDB using a CFD code in order to calculate the disk speed, which is then compared to measurements. Instead Dousti *et al.* [6] obtain similar results using a THD approach incorporating Reynolds-PDE as well as energy equation. Both of them neglect rotor dynamics including tilting motions of shaft or floating disk, which are considered in the work of Ziese *et al.* [12]. On the other hand, the mutual hydrodynamic interactions between axial and radial fluid films are neglected there.

1.2. Outline

In order to predict the vibrational behaviour of a rotor with such a bearing, the bearing properties in terms of nonlinear and state dependent stiffness and damping have to be taken into account. Therefore, the coupled pressures in the three fluid films are calculated depending on the actual kinematics of the bearing elements inside the time integration of equations of motion. The describing Reynolds-PDE is solved numerically with FVM using a suitable cavitation algorithm. The Elrod-Adams model [13] has been established as state of the art in this field. Hence, a current version [14, 15] developed by the authors is adapted to FFDBs ensuring both a fast and accurate solution due to its regularised formulation. Finally, the obtained solution is embedded in a time integration scheme to handle the rotor equations of motion.

Starting with a rotor supported by a combined bearing, the influence of the coupling at the interface between the fluid films is studied. Finally, this task is extended to a rotor with FFDB in order to determine the influence on the disk speed.

2. BEARING MODEL

Aiming for a rotor dynamic model, the hydrodynamic pressure and the resulting forces are of interest. The time integration process with online hydrodynamics requires a comparatively fast

model. Hence, the Reynolds-PDE is solved on the fluid film domains taking into account the mutual influence due to the interfaces between them.

2.1. Geometry

Since as much as possible of existing routines [12, 14] shall be reused, it is necessary to introduce three single coordinate systems in the fluid domains, cf. Fig. 2 top. On each domain $i = 1 \dots 3$ a gap function h_i has to be defined in local z_i direction as a function of the remaining coordinates and the degrees of freedom x_{fd} , y_{fd} and z_{fd} , cf. Fig. 2 bottom.

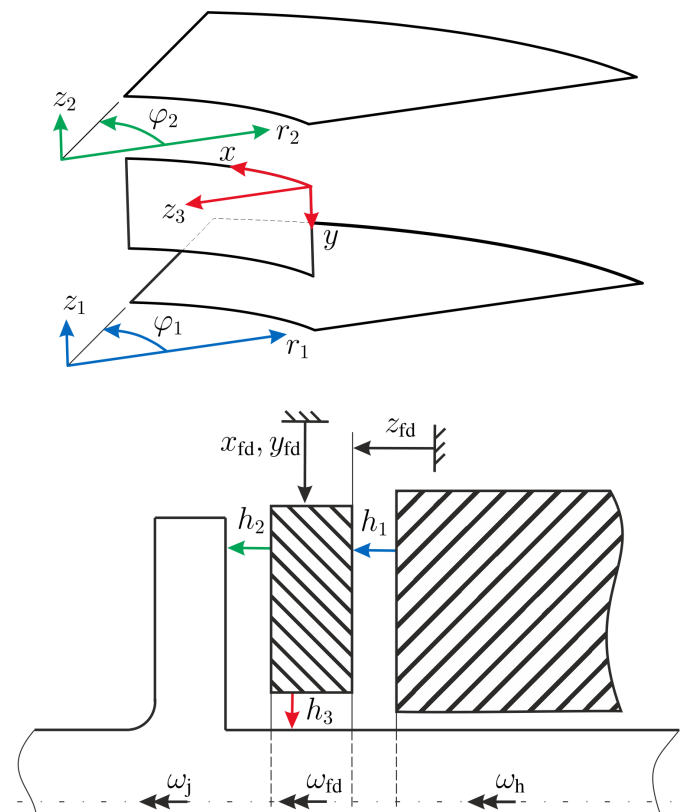


Fig. 2. Domains and coordinate systems for solving Reynolds-PDE in a combined bearing or a FFDB (top) and sectional view of fluid film gap in FFDB with translational degrees of freedom and rotational velocities (bottom)

In real application of FFDB, the shaft and thereby the thrust collar are subject to tilting motions due to shaft displacement as well as shaft bending. For the sake of simplicity, the surfaces of thrust collar, disk and housing are kept parallel here. Thus, the restoring moments due to tilting are neglected, which underestimates the bearings damping capabilities [16]. Furthermore, the tilting stiffness is neglected, which can affect the rotor eigenbehaviour, concerning especially modes with conical shape. With this assumption, the gap functions read

$$h_1(r_1, \varphi_1) = z_{fd} + \begin{cases} h_{1,0} & \text{in flat part} \\ h_{1,0} + c_{wed} - \beta_{wed} r_1 \varphi_1 & \text{in tapered part} \end{cases} \quad (1)$$

$$h_2(r_2, \varphi_2) = -z_{fd} + \begin{cases} h_{2,0} & \text{in flat part} \\ h_{2,0} + c_{wed} - \beta_{wed} r_2 \varphi_2 & \text{in tapered part} \end{cases} \quad (2)$$

in the axial films and

$$h_3(x) = c_{rad} - x_{fd} \cos(x) - y_{fd} \cos(x) \quad (3)$$

in the radial film. Therein, c_{wed} and β_{wed} according to Fig. 3 denote the wedge height and the associated wedge angle respectively, while c_{rad} describes the radial clearance between floating disk and shaft. The initial clearance in the axial fluid films is named $h_{1,0}$ and $h_{2,0}$ respectively. The radial gap between the floating disk and the shaft is related to the translational displacements x_{fd} and y_{fd} of the floating disk. Furthermore the rotational speeds of the journal ω_j , the floating disk ω_{fd} and the housing ω_h are introduced, cf. Fig. 2 bottom.

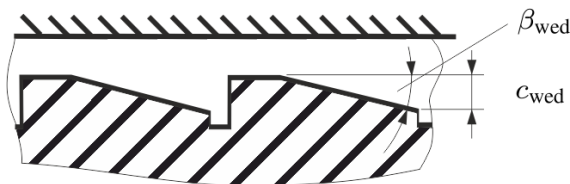


Fig. 3. Parameters of axial fluid film geometry

2.2. Reynolds-PDE

The Reynolds-PDE for a radial journal bearing with the Elrod cavitation model from [14] reads

$$\left[\frac{\partial}{\partial X} \left(\frac{H^3}{12\bar{\eta}} \frac{\partial \Pi}{\partial X} \right) + \frac{\partial}{\partial Y} \left(\frac{H^3}{12\bar{\eta}} \frac{\partial \Pi}{\partial Y} \right) - \frac{\partial H}{\partial X} - \frac{\partial H}{\partial T} \right] g + \left[\frac{\partial((\Pi+1)H)}{\partial X} + \frac{\partial((\Pi+1)H)}{\partial T} \right] (g-1) = 0. \quad (4)$$

Therein, the relations

$$H = \frac{h}{c^*}, \quad X = \frac{x}{r^*}, \quad Y = \frac{y}{r^*}, \quad \bar{r} = \frac{r}{r^*}, \quad \bar{\eta} = \frac{\eta_{liq}}{\eta^*}, \quad (5)$$

$$P = \frac{p}{\eta^* |\omega_m|} \left(\frac{c^*}{r^*} \right)^2, \quad T = t |\omega_m|, \quad \omega_m = \frac{\omega_j + \omega_{fd}}{2}$$

are used to obtain adequate normalised equations. For the axial fluid film the Reynolds equation is expressed in cylindrical coordinates and furthermore centrifugal forces have to be considered [17] leading to the following form

$$\left[\frac{1}{\bar{r}} \frac{\partial}{\partial \bar{r}} \left(\bar{r} \frac{H^3}{12\bar{\eta}} \frac{\partial \Pi}{\partial \bar{r}} \right) + \frac{1}{\bar{r}^2} \frac{\partial}{\partial \varphi} \left(\frac{H^3}{12\bar{\eta}} \frac{\partial \Pi}{\partial \varphi} \right) - \frac{1}{\bar{r}} \frac{\partial(H u_{\varphi m})}{\partial \varphi} - \frac{1}{\bar{r}} \frac{\partial(\bar{r}^2 a_c H^3)}{\partial \bar{r}} - \frac{\partial H}{\partial T} \right] g + \left[\frac{1}{\bar{r}} \frac{\partial((\Pi+1)(H u_{\varphi m}))}{\partial \varphi} + \frac{1}{\bar{r}} \frac{\partial((\Pi+1)(\bar{r}^2 a_c H^3))}{\partial \bar{r}} + \frac{\partial((\Pi+1)H)}{\partial T} \right] (g-1) = 0 \quad (6)$$

$$\text{with } a_c = \frac{\rho}{\eta} \frac{c^{*2}}{\omega_m} \left[\frac{\omega_j^2 + \omega_{fd}^2}{40} + \frac{\omega_j \cdot \omega_{fd}}{60} \right].$$

In equations (4) and (6), the function $g(\Pi) = 0 \dots 1$ serves as switch between pressurised and cavitation domain. Simultaneously the common unknown Π , changes its meaning from pressure p to fluid film content ϑ

$$\Pi \stackrel{!}{=} \begin{cases} \vartheta - 1 & (x, y) \in \Omega_{\vartheta} \\ P & (x, y) \in \Omega_p \end{cases} \Leftrightarrow \begin{cases} \vartheta(x, y) = (1-g)\Pi(x, y) + 1 \\ P(x, y) = g\Pi(x, y) \end{cases} \quad (7)$$

according to the value of the switch function g .

2.3. Full-floating disk thrust bearing

In order to calculate the pressure field in the fluid films of a FFDB, equations (4) and (6) have to be combined. Two interfaces exist: the first (I_1) between outer axial film h_1 and the radial film h_3 and the second (I_2) between inner axial film h_2 and the radial film h_3 , cf. Fig. 2 bottom.

In I_2 , it is obviously that the pressure will be identical at that interface. Besides, in the interface I_1 an additional volume flow can occur between shaft and housing, leading to a pressure drop, which depends on the geometry in the interface region as well as the gap between shaft and housing. Thus, a large and short gap will yield ambient pressure in the interface (I_1), while a long and small gap will act as sealing. In the limiting case of an ideal sealing, identical pressure can be also assumed in (I_1). However, for the sake of simplicity this leakage flow will be neglected, but can be later considered easily. Consequently, equality of film content is assumed at the interfaces, which in the end yields the coupling conditions

$$\Pi_1 = \Pi_3 \quad \text{on } \partial I_1 \quad \text{and} \quad (8)$$

$$\Pi_2 = \Pi_3 \quad \text{on } \partial I_2. \quad (9)$$

Additionally, the following boundary conditions

$$\Pi = \Pi_{amb} \quad \text{on } \partial \Omega_p^{amb} \quad \text{and} \quad (10)$$

$$\frac{\partial \Pi}{\partial Y} = 0 \quad \text{on } \partial \Omega_{\vartheta}^{amb} \quad (11)$$

have to be fulfilled at the outer radii of the axial films, while

$$\Pi = \Pi_{\text{inlet}} \quad \text{on} \quad \partial\Omega_p^{\text{inlet}} \quad (12)$$

is applied at the pressure inlet, typically positioned at the housing.

A numerical solution is usually obtained by discretisation of the Reynolds-PDE on the associated domain using FDM, FVM, FEM or related methods. While FEM allows in the context of the interfaces for comparatively easy implementation, it shows some disadvantages in handling the cavitation (necessity of SUPG or artificial diffusion). Instead, re-using existing FVM code in our case was the more promising variant. The drawback is the necessity to arrange explicitly a connection between the domains based on the assumed equality of pressure in the interface regions. This can be achieved either via Lagrange multipliers (leading to additional equations) or a penalty strategy (with the need to determine an empirical penalty parameter). The third method, which was used here, is to implement an interface element, which is associated in equal parts to the radial film and to the axial film.

Using the usual FVM approach

$$\int_{\bar{r}_0}^{\bar{r}_n} \int_{\varphi_w}^{\varphi_e} \mathcal{L}_{\text{ax}}(\Pi) \, d\Omega, \quad (13)$$

$$\int_{\bar{r}_s}^{\bar{r}_0} \int_{\varphi_w}^{\varphi_e} \mathcal{L}_{\text{rad}}(\Pi) \, d\Omega \quad (14)$$

the equations (4) and (6) written as differential operator $\mathcal{L}(\Pi)$ are processed for the associated parts of the interface elements, cf. Fig. 4 left. Details of numerical implementation concerning the application of FVM to the Reynolds PDE are given in [15]. Finally, assembling the contributions of all domains the sparse system

$$\underline{A}(p) \underline{p} = \underline{r} \quad (15)$$

of equations with nonlinear character results, cf. Fig. 4 right. The nonlinearity results from the task to find the correct shares

of pressurised and cavitational regions, which is expressed by the switch function. The choice of a Sigmoid-type switch function

$$g(\Pi) = \frac{1}{\pi} \arctan\left(\frac{\Pi}{1-\Pi^*}\right) + \frac{1}{2} \quad (16)$$

enables a finite volume to be part of both regions at the same time, leading to a smooth transition between them. Thus, on the one hand convergence is ensured and on the other hand finding the solution is accelerated by the possibility to use a Newton-Raphson algorithm [14].

2.4. Fluid film forces

In preparation for the application of the bearing model within the equations of motion in Section 4, the forces and torques due to the pressure distribution are determined by integration. The force vector and the drag torque of the journal bearing part read

$$\underline{f}_{\text{rad}} = \int_0^{2\pi} \int_0^b \begin{pmatrix} \cos \varphi \\ \sin \varphi \\ 0 \end{pmatrix} p \, dx dy \quad (17)$$

and

$$M_{\text{rad}} = r \int_0^{2\pi} \int_0^b \frac{1}{2} \frac{\partial p}{\partial x} h + \eta_{\text{liq}} \vartheta r \frac{\omega_j - \omega_{fd}}{h} \, dx dy, \quad (18)$$

while in an axial fluid film

$$\underline{f}_{\text{ax}} = \int_0^{2\pi} \int_{r_i}^{r_a} \begin{pmatrix} 0 \\ 0 \\ p \end{pmatrix} r \, d\varphi dr \quad (19)$$

and

$$M_{\text{ax}} = \int_0^{2\pi} \int_{r_i}^{r_a} \frac{1}{2} \frac{\partial p}{\partial \varphi} h r + \eta_{\text{liq}} \vartheta r^2 \frac{\omega_j - \omega_{fd}}{h} \, d\varphi dr \quad (20)$$

are applied respectively.

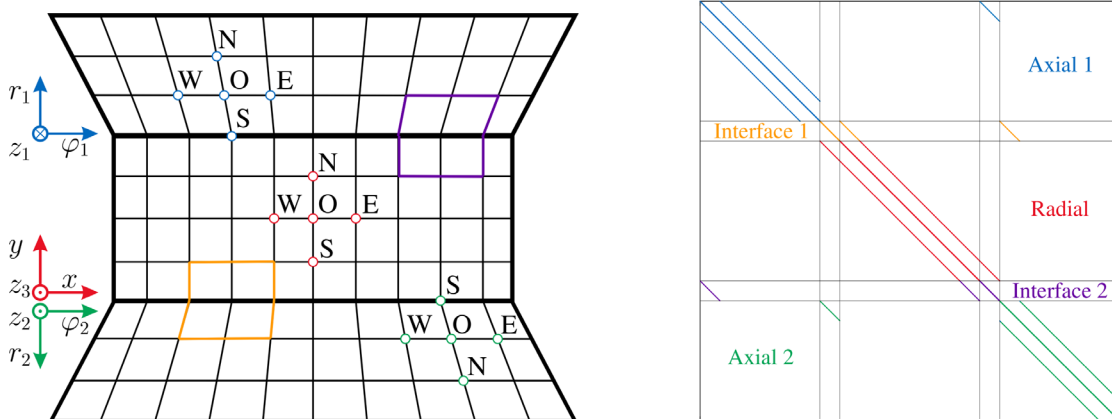


Fig. 4. Mesh in the domains with different coordinates/local stencil orientations and highlighted interface elements in yellow and purple (left) and resulting structure of system matrix including position of interface elements (right)

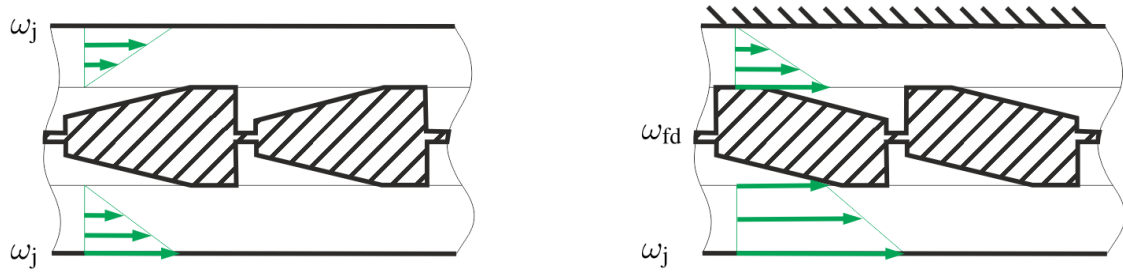


Fig. 5. Different orientation of wedge profiles in axial fluid films for combined bearing (left) and full floating disk bearing (right) to ensure fluid transport into converging gap

3. COUPLED VS. UNCOUPLED SOLUTION UNDER STATIONARY CONDITIONS

In this section, the influence of the developed interface element on the solution, more precisely on the pressure and film content as well as on subordinated quantities like forces and torques is studied. In an uncoupled solution the boundary conditions (10) and (11) are applied additionally on the inner radii of the axial films and on both axial borders of the radial film, which leads to the usual parabolic form of the pressure distribution in transverse direction. Contrarily, the coupling yields significant pressure values on the interfaces, which increases the mean pressure

drastically, cf. Fig. 7. The associated film content is displayed in Fig. 8.

With regard to the application in a rotor dynamic model, the fluid film forces and torques come to the focus. Hence, the lateral displacement in the stationary combined bearing model was varied, cf. Fig. 6. In the uncoupled case, the radial force and the associated angle are of course independent from z_{fd} , but even in center position $z_{fd} = 0$, the force rises clearly and the direction of its action is also influenced due to the coupling. The absolute value of the force is increased by increasing the lateral displacement, because the small axial gap in the second

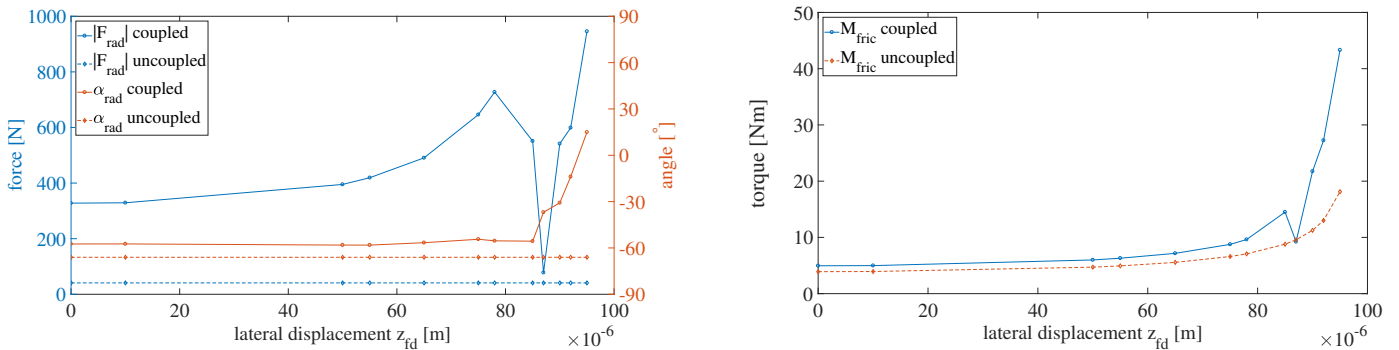


Fig. 6. Influence of coupling due to interface element for different values of lateral displacement: absolute radial forces F_{rad} and associated angle α_{rad} (left), drag torque (right). Model parameter according to Fig. 7

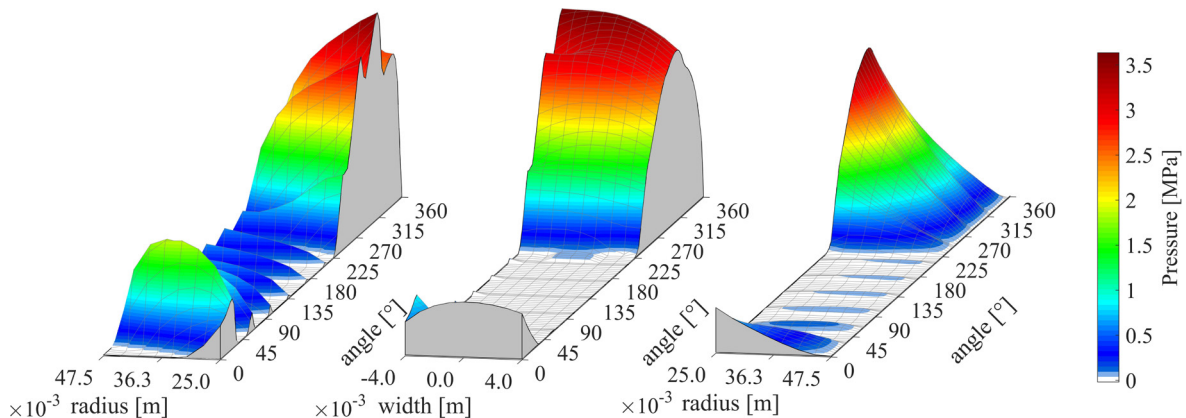


Fig. 7. Coupled solution of Reynolds-PDE: Pressure in the fluid films of a combined bearing with 10 segments. Oil supply is located in the center part at $\varphi = 225^\circ$ with $p_{in} = 0.1$ MPa. The asymmetry results from the lateral displacement of the journal w.r.t. the center part. Parameter: $h_{10} = h_{20} = 100$ μm , $z_{fd} = 50$ μm , $c_{wed} = 85$ μm , $\alpha_{wed} = 27^\circ$, $\alpha_{flat} = 5^\circ$, $c_{rad} = 40$ μm , $\varepsilon = e/c_{rad} = 0.25$, $\omega_{fd} = 0$, $\omega_j = \omega_{housing} = 5000$ rad/s, $\eta = 0.012$ Pa s

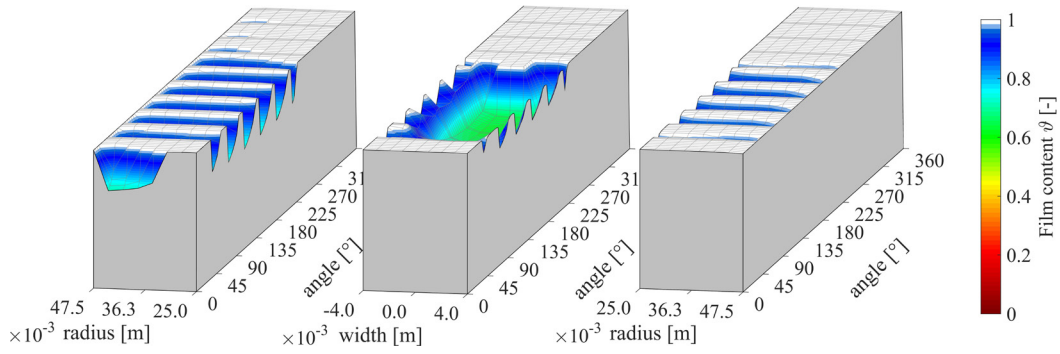


Fig. 8. Coupled solution of Reynolds-PDE: film content in the fluid films of a combined bearing. Parameter according to Fig. 7

axial film leads to high pressure there. Finally, this causes a volume flow into the radial journal yielding the increase in radial force. In the region of high lateral displacement, the amount of volume flow transferred to the radial film is high enough to fill even the cavitation region there. Hence, the pressure in the radial film is more or less equally distributed in the radial film. This leads to the observed force drop at $z_{fd} = 88 \mu\text{m}$, cf. Fig. 6 left, while at the same time the direction of force changes.

In a FFDB, the drag torques obviously play a major role. Due to the coupling, the drag torques are slightly larger for moderate lateral displacement, while the difference becomes larger at maximal displacement, cf. Fig. 6 right.

4. EQUATIONS OF MOTION

A first step towards the application of the described bearing model in a transient simulation of a real rotor is to implement the hydrodynamics (equations (15)–(20)) in the equations of motion of a rigid rotor

$$\begin{pmatrix} m & 0 & 0 & 0 \\ 0 & m & 0 & 0 \\ 0 & 0 & m & 0 \\ 0 & 0 & 0 & J_{zz} \end{pmatrix} \begin{pmatrix} \ddot{x} \\ \ddot{y} \\ \ddot{z} \\ \ddot{\varphi} \end{pmatrix} + \begin{pmatrix} -U\dot{\varphi}^2 \cos \varphi \\ -U\dot{\varphi}^2 \sin \varphi \\ 0 \\ 0 \end{pmatrix} = \begin{pmatrix} F_x \\ F_y \\ F_z \\ M_z \end{pmatrix} - \begin{pmatrix} F_{rad,x} \\ F_{rad,y} \\ -F_{ax,z,1} + F_{ax,z,2} \\ M_{ax,1} + M_{ax,2} + M_{rad} \end{pmatrix} \quad (21)$$

under unbalance U and external loads (F_x, F_y, F_z, M_z) . The rotor is allowed to move in all translational directions (x, y, z) as well as to rotate around the z -axis (angle φ). Finally, m denotes the rotor mass and J_{zz} its mass moment of inertia w.r.t. z -axis.

This set of equations is then solved by means of time integration using an ODE-Solver, whereas the Reynolds PDE is solved and resulting forces and the drag torques are calculated in each time step. To close the loop between hydrodynamics and mechanics, the rotors axial coordinate z enters in the gap functions (1) and (2), while the radial displacements x and y contribute to the radial gap (3). Furthermore, the hydrodynamic active speed ω_m in equation (4) as well as in equation (6) is calculated from the current rotor speed. Finally, the time depen-

dant term in the Reynolds–PDE has to be handled during time integration, which is here achieved by an explicit Euler step as proposed in [18] and described at length in [15].

4.1. Combined bearing

If the rigid rotor in equation (21) is assumed to represent the journal and the rotational speeds according to Fig. 2 are set as follows

$$\omega_j = \omega_h = \dot{\varphi} \quad \text{and} \quad \omega_{fd} = 0, \quad (22)$$

the model of a combined bearing with two rotating collars and a fixed shell in its center results. Furthermore, the profiles in both axial films are located on the fixed part and the wedges are orientated identically referring to the shaft direction of rotation, cf. Fig. 5 left.

Figure 9 illustrates the orbits of both solutions, coupled and uncoupled, under an unbalance $U = 0.9 \text{ g mm}$, a radial load of $F_y = 5000 \text{ N}$ and varying axial loads, while the rotational speed was kept constant. The remaining parameter are chosen according to Fig. 7. Both solutions show qualitatively an identical behaviour, as one would expect from the outer loads, but the location and the form of the final orbit differ significantly. It can be concluded that the coupled solution leads to higher radial stiffness.

Furthermore, the axial load F_z affects the orbit location. In the coupled case, an increase of axial load shifts the orbit center to lower eccentricities. Apparently, high pressure in the axial film region yields an also high pressure level in the radial film, which results in an increase of radial stiffness.

Simultaneously, the coupling due to the interface elements shows an influence on the axial displacements. According to Table 1, the combined bearing is able to carry a larger axial load in the coupled case.

Table 1

Different relative axial positions $\bar{z} = z_{fd}/h_{10}$ of journal at end of time integration process, cf. Fig. 9, due to different axial loads. Influence of coupling due to interface elements

	$F_z = 0 \text{ N}$	$F_z = 1000 \text{ N}$	$F_z = 5000 \text{ N}$	$F_z = 10000 \text{ N}$
coupled	0.0000	0.3347	0.6611	0.7546
uncoupled	0.0000	0.5101	0.8338	–

Analysis of dynamical behaviour of full-floating disk thrust bearings

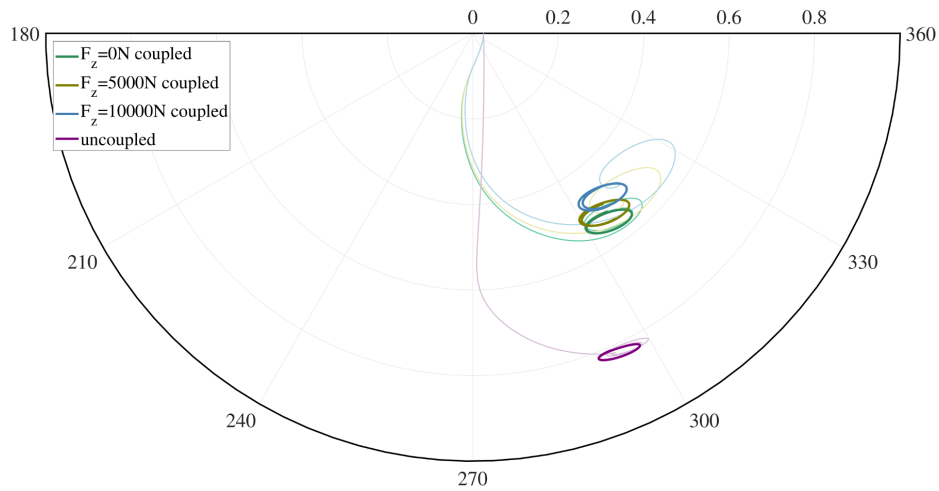


Fig. 9. Influence of coupling due to interface elements on the transient behaviour on a combined bearing model. Bearing parameter according to Fig. 7, Static load applied $F_y = 5$ kN, unbalance $U = 0.9$ g mm, mass $m = 0.3$ kg. Additionally, the influence of axial load F_z can be seen in the coupled case

4.2. FFDB

If in contrast to Section 4.1, the equations of motion (21) shall model an FFDB, a different set of boundary conditions is necessary. The left collar performs a constant rotation with ω_j , while the right collar is assumed to be fixed $\omega_h = 0$. Since the rigid rotor now represents the floating disk, its rotational speed $\omega_{fd} = \dot{\varphi}$ is determined by the drag torques of all fluid films, which themselves depend on the outer loads (F_{ax} and F_{rad}) as well as on initial conditions.

Hence in the two axial films a different effective rotational speed ω_m results. Since the axial film profiles are still located to the (rotating) floating disk, their orientation needs to be opposing in order to generate hydrodynamic pressure, cf. Fig. 5 right. Usually an FFDB is radially loaded only by gravity and

unbalance. Hence, low radial Sommerfeldnumber results and thus may indicate a tendency to whirl motions.

According to these circumstances the model was set up: there is no static radial load but the gravity force of the disc and the unbalance was set to $U = 0.4$ g mm. Since no outer axial load acts on the disc itself, $F_z = 0$ is assumed. Nevertheless due to sum of the axial clearance in both gaps (which is kept constant), an internal axial load is generated. Because the FFD is able to translate in z-direction, during time integration a position is found, where the axial loads F_{ax1} and F_{ax2} are equal in both gaps.

In Fig. 10 the solutions at the end of time integrations process are compared for different values of axial sum clearance. It is clear, that with decreasing clearance values the axial load

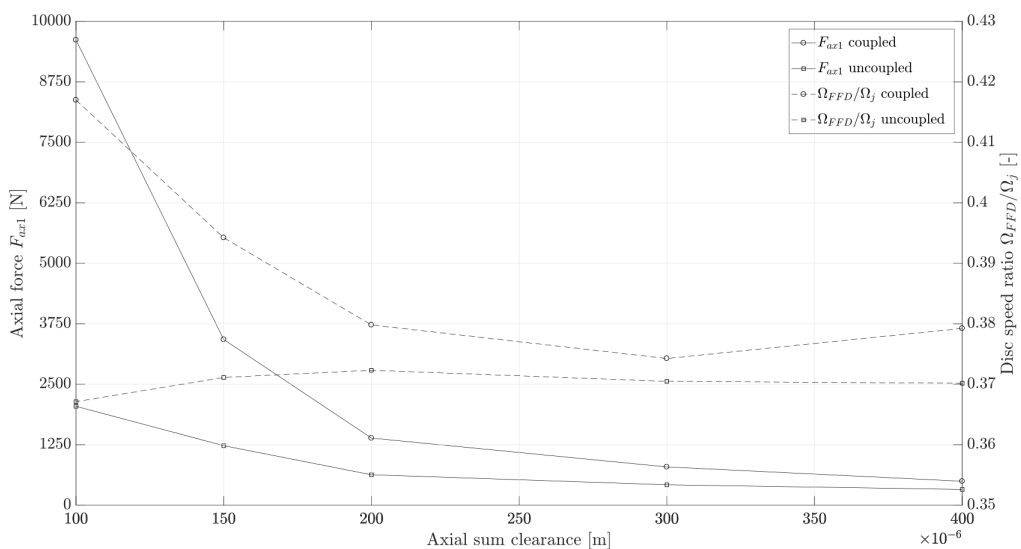


Fig. 10. Influence of coupling due to interface elements and axial sum clearance on axial force and disc speed ratio. Bearing geometry parameter according to Fig. 7. Force and ring speed ratio are nearly constant in the uncoupled case, while they are increasing with lower sum clearance in the coupled case

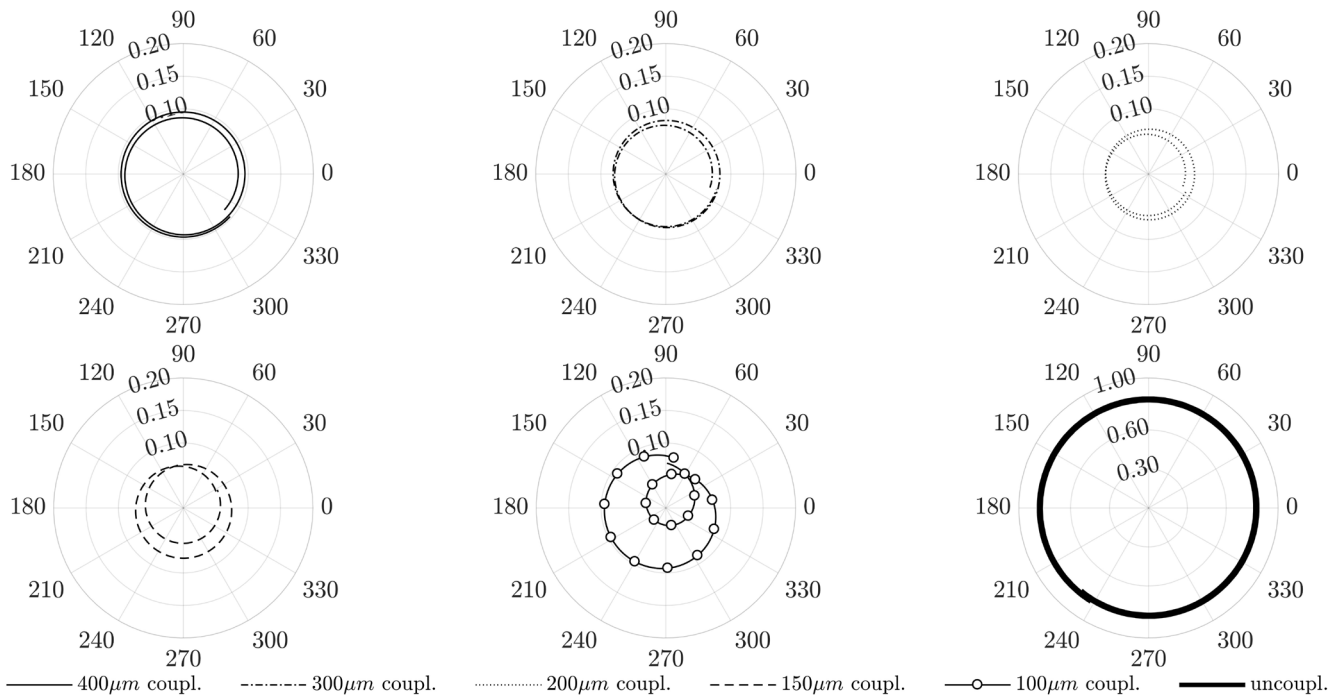


Fig. 11. Influence of coupling due to interface elements and axial sum clearance on orbit of FFD. Bearing geometry parameter according to Fig. 7

capacity rises. Analogously to the combined bearing model, the coupling due to the interface elements leads to a further increase in the axial load capacity. In addition to the load capacity, the drag torques are also influenced by the clearance, which results in a different speed ratio of the disc. The values for Ω_{FFD}/Ω_j is found to be in the range of 0.38...0.42 here, which is in coincidence with [5].

As mentioned above, the FFD tends to whirling motions, Fig. 11, which are amplified by decreasing axial clearance or increasing axial loads in the coupled case, which is indicated by the change of orbit form from circular to the typical whirl shape. Contrarily, in the uncoupled case the form and size of the orbit are not influenced by axial sum clearance. Furthermore, in the case of this particular parameter set the orbit is much larger compared to the coupled solutions, but this can't be generalised.

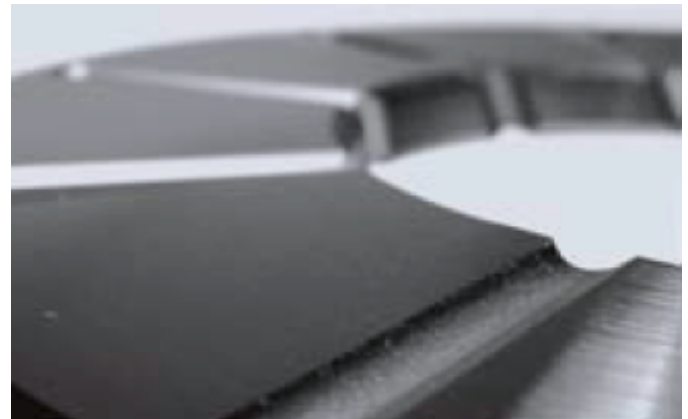


Fig. 12. Different floating disk designs: adjacent axial and radial fluid film area [19] (top) and additional pocket on interface between axial and radial fluid film [20] (bottom)

5. CONCLUSION AND OUTLOOK

The paper at hand addresses the consideration of a full floating ring thrust bearing in a transient rotor dynamic simulation using an online solution of the Reynolds-PDE. Hence, a coupled bearing model consisting of two axial and the center radial fluid film was derived. Cavitation was handled with a regularised Elrod algorithm, which was developed by the authors earlier for both journal and thrust bearings. The hydrodynamic model was then embedded in the time integration of a rigid rotor equations of motion in order to demonstrate its applicability. The algorithm is generally able to handle transient processes due to run-up, transient loads or other abrupt occurring circumstances. Without loss of generality, the calculations are restricted to nearly steady-state conditions.

The results show a clear influence due to the coupling of the fluid films on the pressure distribution and the subordinated quantities like forces and drag torques. It is clear that the model assumption of equal pressures at the interface builds a theoretical limiting case. In real applications, often comparatively large grooves are placed at the interface (Fig. 12 right) and at least at the housing side axial fluid film a certain amount of volume flow is lost due to the gap between housing and journal, cf. Fig. 2 right. To consider these circumstances, further equations have to be added to the model. Moreover, thermohydrodynamic effects have also a significant influence on the temperatures of the bearing and the fluid. Hence, in future simulations the energy equation should be considered as well, e.g. in an analogous form to [21]. However, even the present model can be included in a rotor dynamic simulation of a turbocharger rotor, where the shaft is modeled via finite element beams. For this sake, the restoring moments due to tilting motion of thrust collar and full floating disk need to be considered. Furthermore, the orbit of the shaft causes some kind of base excitation on the FFD, while at the same time the whirl motion of the FFD can be transferred to the shaft leading to unwanted subsynchronous vibrations.

ACKNOWLEDGEMENTS

The results were partially generated in the framework of the project WO 2085/2–2 “Einfluss der Axiallagerdynamik auf das Rotorverhalten: Transiente Analyse unter Berücksichtigung der Kavitation sowie der Kopplung von axialen und radialen Schmierfilmen”, which is supported by the DFG (Deutsche Forschungsgemeinschaft/German Research Foundation). This support is gratefully acknowledged.

REFERENCES

- [1] M.C. Shaw and T.J. Nussdorfer, “An analysis of the full-floating journal bearing,” NACA, Tech. Rep. RM-E7A28a, 1947.
- [2] C. Kettleborough, “Frictional experiments on lightly-loaded fully floating journal bearings,” *Aust. J. Appl. Sci.*, vol. 5, pp. 211–220, 1954.
- [3] J. Dworski, “High-speed rotor suspension formed by fully floating hydrodynamic radial and thrust bearings,” *J. Eng. Gas Turbines Power*, vol. 86, no. 2, pp. 149–160, 1964.
- [4] M. Harada and J. Tsukazaki, “The steady-state characteristics of a hydrostatic thrust bearing with a floating disk,” *J. Tribol.*, vol. 111, no. 2, pp. 352–357, Apr 1989, doi: 10.1115/1.3261921.
- [5] M. Fischer, A. Mueller, B. Rembold, and B. Ammann, “Numerical investigation of the flow in a hydrodynamic thrust bearing with floating disk,” *J. Eng. Gas Turbines Power*, vol. 135, 2013, doi: 10.1115/1.4007775.
- [6] S. Dousti and P. Allaire, “A thermohydrodynamic approach for single-film and double-film floating disk fixed thrust bearings verified with experiment,” *Tribol. Int.*, vol. 140, p. 105858, Dec 2019.
- [7] H. Engel, “Berechnung der Strömung, der Drücke und Temperaturen in Radial-Axialbund-Gleitlagern mit Hilfe eines Finite-Elemente-Programms,” Ph.D. thesis, Universität Stuttgart, 1992.
- [8] T. Hagemann, H. Blumenthal, C. Kraft, and H. Schwarze, “A study on energetic and hydraulic interaction of combined journal and thrust bearings,” in *Proceedings of ASME Turbo Expo 2015: Turbine Technical Conference and Exposition*, no. GT2015–43460, 2015, pp. 1–11.
- [9] G.H. Jang, S.H. Lee, and H.W. Kim, “Finite element analysis of the coupled journal and thrust bearing in a computer hard disk drive,” *J. Tribol.*, vol. 128, pp. 335–340, 2006, doi: 10.1115/1.2162918.
- [10] G. Xiang, Y. Han, R. Chen, J. Wang, X. Ni, and K. Xiao, “A hydrodynamic lubrication model and comparative analysis for coupled microgroove journal-thrust bearings lubricated with water,” *Proc. Inst. Mech. Eng., Part J: J. Eng. Tribol.*, vol. 234, no. 11, pp. 1755–1770, Nov 2019.
- [11] J.-C. Luneno, “Coupled vibrations in horizontal and vertical rotor-bearings systems,” Ph.D. thesis, Luleå University of Technology, 2010.
- [12] C. Ziese, C. Daniel, E. Woschke, and H. Mostertz, “Hochlaufsimulation eines semi-floating gelagerten ATL-Rotors mit schwimmender Axiallagerscheibe,” in *14. Magdeburger Maschinenbautage (24.–25.09.2019)*, Sep. 2019, pp. 105–112.
- [13] H.G. Elrod, “A cavitation algorithm,” *J. Tribol.*, vol. 103, no. 3, pp. 350–354, 1981.
- [14] S. Nitzschke, E. Woschke, D. Schmicker, and J. Strackeljan, “Regularised cavitation algorithm for use in transient rotordynamic analysis,” *Int. J. Mech. Sci.*, vol. 113, pp. 175–183, 2016.
- [15] S. Nitzschke, “Instationäres Verhalten schwimmbuchengelagerter Rotoren unter Berücksichtigung masseerhaltender Kavitation,” Ph.D. thesis, Otto-von-Guericke Universität Magdeburg, 2016.
- [16] C. Daniel, “Simulation von gleit- und wälzgelagerten Systemen auf Basis eines Mehrkörpersystems für rotordynamische Anwendungen,” Ph.D. thesis, Otto-von-Guericke Universität Magdeburg, 2013.
- [17] C. Ziese, E. Woschke, and S. Nitzschke, “Tragdruck- und Schmierstoffverteilung von Axialgleitlagern unter Berücksichtigung von masseerhaltender Kavitation und Zentrifugalkraft,” in *13. Magdeburger Maschinenbautage*, 2017, pp. 312–323.
- [18] A. Kumar and J.F. Booker, “A finite element cavitation algorithm,” *J. Tribol.*, vol. 113, no. 2, pp. 279–284, 1991.
- [19] “MAN turbochargers TCA series floating disk thrust bearing,” <https://turbocharger.man-es.com/docs/default-source/shopware-documents/tca-turbochargerf451d068cde04720bdc9b8e95b7c0f8e.pdf>, accessed: 2020–10–09.
- [20] “KBB turbochargers ST27 series floating disk thrust bearing,” <https://kbb-turbo.com/turbocharger-product-series/st27-series>, accessed: 2020-10-09.
- [21] C. Irmscher, S. Nitzschke, and E. Woschke, “Transient thermohydrodynamic analysis of a laval rotor supported by journal bearings with respect to calculation times,” in *SIRM 2019 – 13th International Conference on Dynamics of Rotating Machines*, 2019, pp. Paper-ID SIRM2019–25.